

MR Acquisition-Invariant Representation Learning

Wouter M. Kouw^{a,*}, Marco Loog^{a,b}, Lambertus W. Bartels^c, Adriënne M. Mendrik^{c,d}

^a*Delft University of Technology, Mekelweg 4, Delft*

^b*University of Copenhagen, Universitetsparken 1, Copenhagen*

^c*University Medical Center Utrecht, Heidelberglaan 100, Utrecht*

^d*Netherlands eScience Center, Science Park 140, Amsterdam*

Abstract

Voxelwise classification is a popular and effective method for tissue quantification in brain magnetic resonance imaging (MRI) scans. However, there are often large differences over sets of MRI scans due to how they were acquired (i.e. field strength, vendor, protocol), that lead to variation in, among others, pixel intensities, tissue contrast, signal-to-noise ratio, resolution, slice thickness and magnetic field inhomogeneities. Classifiers trained on data from a specific scanner fail or under-perform when applied to data that was differently acquired. In order to address this lack of generalization, we propose a Siamese neural network (MRAI-NET) to learn a representation that minimizes the between-scanner variation, while maintaining the contrast between brain tissues necessary for brain tissue quantification. The proposed MRAI-NET was evaluated on both simulated and real MRI data. After learning the MR acquisition invariant representation, any supervised classifier can be applied. In this paper we showed that applying a linear classifier on the MRAI representation outperforms supervised convolutional neural network classifiers for tissue classification when little target training data is available.

Keywords: MRI, acquisition-variation, representation learning, deep neural networks, segmentation, human brain.

*Corresponding author

Email address: W.M.Kouw@tudelft.nl (Wouter M. Kouw)

1. Introduction

Very few of the many medical image analysis algorithms that were proposed in the literature are applicable in clinical practice. One of the reasons for this is the complexity of the medical image data, i.e. the vast amount of variation that is present in this data. A more specific example of this, is brain tissue segmentation in MRI scans. Many automatic methods have been proposed [1, 2, 3, 4, 5, 6, 7, 8], but due to a lack of generalization, large scale use in clinical practice remains a challenge [9]. In order to test the capacity of algorithms to generalize to new data, a representative sample (dataset) is required. This entails identifying all factors of variation in the data that would influence algorithm performance with respect to the medical image analysis task at hand. For brain tissue segmentation in MRI scans, we identify for example subject related variation (i.e. pathology, age, ethnicity, gender) and acquisition related variation (i.e. MR field strength, protocol settings, scanner vendor, artefacts). Supervised voxel classification approaches have been shown to perform well on small data sets [10, 11, 12]. However, in order to ensure generalization, these algorithms should be trained and tested on a sufficiently large representative dataset that covers all possible types of variation. This is practically infeasible since training and testing require not only the MRI scans, but also the manual labels that are used as ground truth. This manual segmentation process is labor intensive and time consuming, and adds another layer of variation as a result of non-standardized manual segmentation protocols and inter- and intra-observer variability. To address this problem, we propose an alternative approach, by learning a representation of the data [13] that is invariant to disturbing types of variation, while preserving the variation relevant for the selected classification task, i.e. clinically relevant variation. By reducing undesired variation, this method has the potential to decrease the number of fully labeled samples required for generalization and enable broader use of voxel classification approaches. In contrast to previously proposed transfer classifiers (variations of SVM, AdaBoost) [14, 10], the proposed learned representation can subsequently

be used as input for any type of supervised classifier.

Learning such a representation can be achieved by marking certain factors of variation as desirable and others as undesired [15]. To this end, we exploit a particular type of neural network, referred to as a Siamese network, that is designed to predict similarity between inputs [16]. Our work was inspired by the work of Hadsell [17] on learning a lighting-invariant representation for airplane images in the NORB [18] dataset. In this paper we aim to provide a proof of principle for learning an MR-acquisition invariant (MRAI-NET) representation for MR brain tissue segmentation.

2. Magnetic Resonance Acquisition-Invariant Network (MRAI-NET)

Neural networks transform data into a representation based on minimizing a loss function. In supervised neural networks, labels are used to determine the loss (error between prediction and label). Many labels are required to learn a task. We aim to use as little labels as possible to learn a representation in which the variation over different methods of acquisition is minimal, without destroying the variation relevant to distinguish between brain tissues.

The proposed network works as follows. Suppose the same subject's scans are acquired in two different ways (A and B): different scanners, different protocols for the same scanner, different receiver coils on the same scanner, or different distances between the subjects and the receiver coils. A tissue patch, for example gray matter, is selected from both scans A and B. The aim is to teach the network that both these patches are gray matter regardless of their acquisition variation. Therefore, we use a loss function that expresses that in the MRAI representation, pairs of samples from the same tissue but from different scanners should be as similar as possible. However, that expression alone would cause all samples to be mapped to a single point and would destroy variation between tissues. To balance out the action of pulling pairs marked as similar together, it is necessary to push other pairs apart [17]. Since we want to maintain the relevant variation between tissues, we additionally express that in the MRAI

representation, pairs from different tissues should retain their dissimilarity. The loss function is described in section 2.1. Section 2.2 describes how pairs of samples are labeled as similar or dissimilar. The Siamese neural network that is used to learn the MRAI representation is described in section 2.3. The network consists of two pipelines with shared weights and a Siamese loss layer that acts on the output layer of the two pipelines (MRAI representation).

2.1. Siamese loss

To find an optimal transformation from input patches to the new representation, we employ a loss function based on the distances between pairs. Pairwise distances are computed through an L^1 -norm; $\|\cdot\|_1$. The L^1 -norm is used, because larger values of p in L^p -norms result in either problems in high-dimensional spaces or problems with the gradient during optimization (see Appendix C). The loss function for the similar pairs consists of the squared distance, $\ell_{\text{sim}}(f | a, b) = (\|f(a) - f(b)\|_1)^2$, to express that large distances are less desirable. The loss function for the dissimilar pairs consists of a hinge loss, where the distance is subtracted from a margin parameter m and the negative values are set to 0: $\ell_{\text{dis}}(f | a, b) = \max(0, m - \|f(a) - f(b)\|_1)$. This expression indicates that pairs that lie close together will suffer a loss, while pairs that are pushed sufficiently far away from each other, i.e. past the margin, will not suffer a loss. We discuss the effect of the margin parameter in Appendix B. The similar and dissimilar loss functions are combined in a *Siamese* loss function [16, 17]:

$$\begin{aligned} \ell(f | \mathcal{D}) &= \sum_i y_i \ell_{\text{sim}}(f | a_i, b_i) + (1 - y_i) \ell_{\text{dis}}(f | a_i, b_i) \\ &= \sum_i y_i \|f(a_i) - f(b_i)\|_1^2 + (1 - y_i) \max(0, m - \|f(a_i) - f(b_i)\|_1) . \end{aligned}$$

Note that this loss is asymmetric, as it penalizes similar patches differently than dissimilar patches.

2.2. Labeling pairs as similar or dissimilar

As described above, assume that the same subject is scanned in two different scanners (A and B). Assume further that we have sufficient manual segmentations (labeled voxels) on scans from scanner A, to train a supervised classifier, but a very limited amount of labels from scanner B, for example 1 labeled voxel per tissue for 1 subject. The data from scanner A will be referred to as the source set, and the data from scanner B as the target set. Let K be the set of tissue labels. The set of patches extracted from Scanner A is denoted $\{(a_{tn})_{n=1}^N$, and the set from scanner B is denoted $\{b_{tm}\}_{m=1}^M$, with t specifying the sample's tissue. Given these two sets of patches, we form sets of similar and dissimilar pairs, with a similarity label y . The following pairs are labeled as similar ($y = 1$) and therefore will be pulled closer together:

- Source patches from the same tissue $k \in K$: $\{(a_{t=k}, a_{t=k})\}$,
- Source and target patches from the same tissue $k \in K$: $\{(a_{t=k}, b_{t=k})\}$,
- Target patches from the same tissue $k \in K$: $\{(b_{t=k}, b_{t=k})\}$.

The subscript $t = k$ selects all patches that belong to tissue k . The following pairs are labeled as dissimilar ($y = 0$) and therefore will be pushed apart:

- Source patches from different tissues $k, l \in K$: $\{(a_{t=k}, a_{t=l})\}$,
- Source and target patches from different tissues $k, l \in K$: $\{(a_{t=k}, b_{t=l})\}$,
- Target patches from different tissues $k, l \in K$: $\{(b_{t=k}, b_{t=l})\}$.

Figure 1 illustrates the process of selecting pairs of patches from different scanners. The pairs are concatenated into a dataset $\mathcal{D} = \{(a_i, b_i, y_i)\}_{i=1}^{N_{\mathcal{D}}}$, where i iterates over the pairs. The number of pairs that can be generated is very large, even when only a small number of patches is available. In total, the number combinations is $N_{\mathcal{D}} = \sum_{k \in K} (N_k + M_k)^2 + \sum_{(k,l) \in \binom{K}{2}} (N_k N_l + N_k M_l + M_k M_l)$, where N_k refers to the number of source patches from the k -th tissue and, likewise, M_k refers to the number of target patches from the k -th tissue. For

example, taking 10 patches of 3 tissues from 4 source scans and 1 patch of 3 tissues from 1 target scan, results in 2784 pairs of patches that can be used for training the deep neural network.

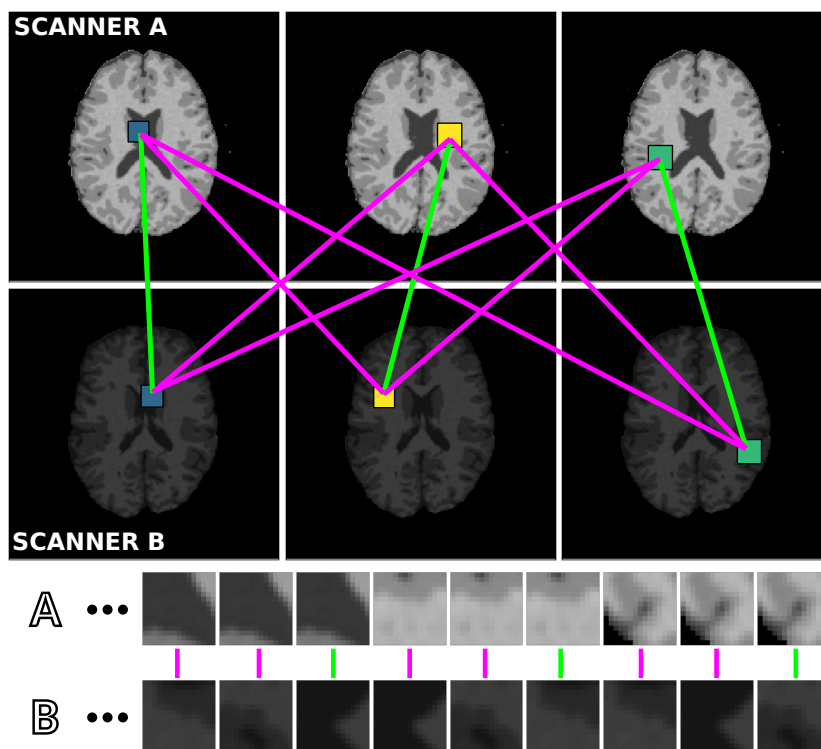


Figure 1: Illustration of extracting pairs of patches from scanner A and B, for cerebrospinal fluid (blue), white matter (yellow), and gray matter (green), respectively. Green lines indicate similar pairs and purple lines indicate dissimilar pairs.

2.3. Network architecture

Figure 2 (top) provides an abstract diagram of the network architecture. The network consists of two pipelines with shared weights and a Siamese loss layer that acts on the output layers (representations). Pairs of patches labeled as similar or dissimilar enter the input layer (black parallelograms) after which they are transformed, through the two pipelines (blue rectangles), into the new representation (red squares). The two pipelines share their weights, which means they

are constrained to perform the same transformation. The Siamese loss function (section 2.1) is computed based on the new representations (red squares) and the error signal is propagated back through the network, adjusting the network weights.

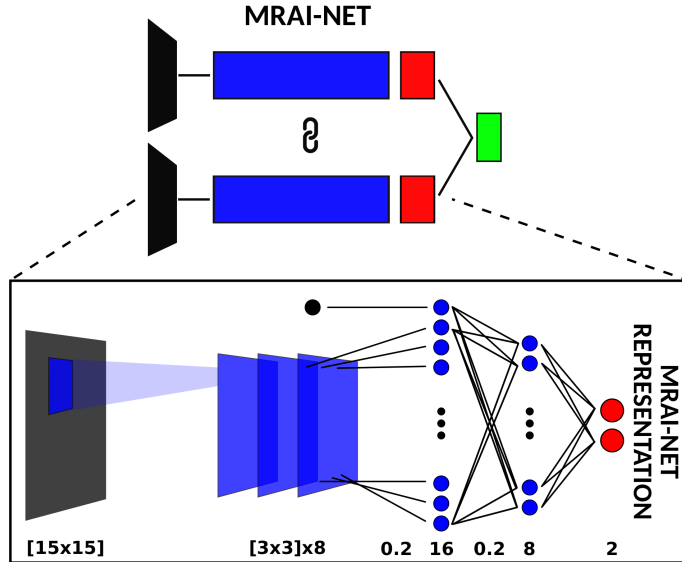


Figure 2: Schematic representation of the MR acquisition invariant neural network (MRAI-NET) architecture. **Top:** Siamese network architecture: pairs of patches are fed into two neural network pipelines resulting in two representations (red) used as input to compute the Siamese loss (green). The weights in the pipelines are shared (chain symbol) and updated according to the Siamese loss comparing the two representations. When the network converges, the two representations are similar and an MRAI representation is learned. **Bottom:** Diagram of a neural network pipeline: the input layer (black) consists of a patch (15×15). Convolutions (8 kernels of 3×3) with max-pooling (2×2) are performed on the patch and the resulting activation maps are unraveled into a vector representation. This vector representation is appended with a scanner identification variable and densely mapped to the first hidden layer (16-dimensional), with a dropout noise of 0.2. This hidden layer is then densely mapped, with again a dropout of 0.2, to a second hidden layer (8-dimensional) and finally densely mapped to the output representation (2-dimensional for visualization).

Figure 2 (bottom) illustrates the pipeline architecture. The black square indicates the input patches (15×15 pixels in this proof of principle). The first

hidden layer then consists of 8 convolutional kernels of size 3×3 with a max-pooling layer of size 2×2 . The output of these operations is flattened and a scanner identification variable is appended. The scanner ID ensures that regions of different tissues in different scanners do not overlap in the input space, e.g. that source gray matter patches can be differentiated from target white matter patches even if they have the same appearance. This variable can consist of the acquisition-protocol parameters but any consistent labeling of scanners is sufficient. For example, for a situation with one source and one target scanner, a 0/1-encoding suffices. The flattened and pooled convolutional layer output along with the appended scanner identification are then densely mapped to a 16-dimensional representation. A dropout noise of size 0.2 is set for each edge. This 16-dimensional representation is then densely mapped, again with a dropout of 0.2, to an 8-dimensional representation, which is finally mapped to a 2-dimensional representation. We chose a final representation of 2 dimensions because this allows for scatter plots as visualization.

This proof of principle uses a 4-layer hybrid convolutional-dense network for the pipeline. However, the network architecture can be changed. Variations involve, for example, thinner or wider dense layers, less or more convolutions, and heavier or lighter pooling, but these produce relatively similar results. The most important aspect is the total number of parameters (weights): with an order of magnitude less parameters, the network’s transformation will not be flexible enough and it will not be able to reduce scanner variation without introducing overlap between tissues. On the other hand, if the number of parameters is an order of magnitude larger, the network will find a transformation that is very specific to the given target subject and will not generalize to new target subjects (overfitting).

2.4. Training and applying MRAI-NET for adaptive segmentation

Figure 3 illustrates the MRAI-NET training procedure. Once the MRAI-NET is trained and an MR acquisition-invariant representation is learned, it can be used as a preprocessing step for tissue segmentation (Figure 4). Because of the

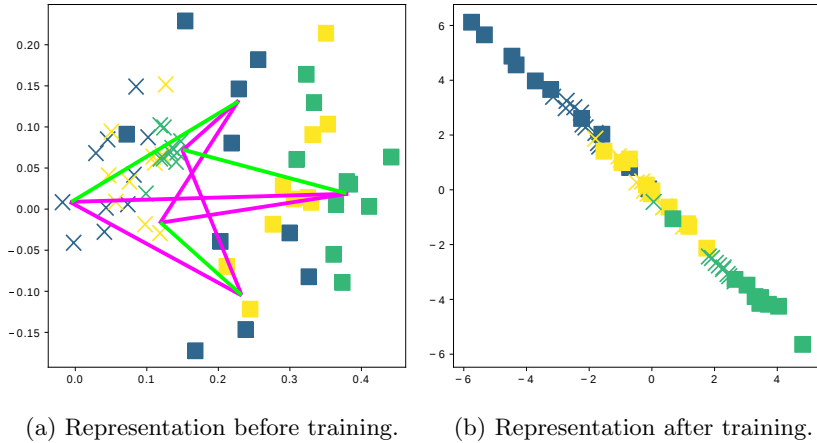


Figure 3: Illustration of the MRAI-NET training procedure: the network pulls the similar pairs (green lines) closer together and pushes dissimilar pairs (purple lines) apart until it learns a representation in which the variation between scanners is minimal while the variation between tissues is maintained.

shared weights, either one of the pipelines can be used to transform the input patches into the MRAI representation. Input patches from both the source and target scanner can be fed to the network, and any supervised classifier can subsequently be trained to distinguish tissues in the acquisition-invariant representation. Once the supervised classifier is trained, both the trained MRAI-NET and the trained supervised classifier are used to segment a new image. This is done by feeding a new patch through the MRAI-NET and let the tissue classifier predict the label in the MR acquisition invariant space. In this way, the MRAI-NET acts as a preprocessing step to ensure that acquisition-based variation does not affect the tissue classifier.

3. Evaluating MRAI-NET

Since the aim of the MRAI-NET is to preserve variation between tissues while reducing the MR acquisition related variation, two different measures of performance are used to evaluate MRAI-NET. MR acquisition invariance is measured with the proxy \mathcal{A} -distance that measures the distance between the source and

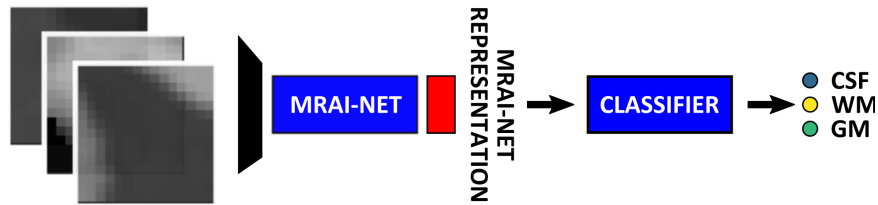


Figure 4: A dataset of tissue-labeled single patches is fed through MRAI-NET and represented in the acquisition-invariant space. Subsequently, a classifier is trained to distinguish tissues. A new image is decomposed into patches and fed through the network as well. The trained tissue classifier then makes a prediction for each patch. The predictions are then reshaped back into an image, resulting in the tissue segmentation.

target scanner patches, as described in section 3.1. The preservation of tissue variation is measured using the tissue classification performance, and compared to supervised classification with CNN (Section 3.2). Section 3.3 describes the simulated (Brainweb 1.5T, Brainweb3T) and real data (MRBrainS) used for the experiments. For each experiment a source and target domain was specified. Four source subjects (100 random patches per tissue) and 1 target subject (1-1000 patches per tissue depending on experiment) were used for training. Four independent target subjects (100 random patches per tissue) were used for testing. Two experiments were set-up: 1) Only 1 patch per tissue from the target domain subject is used for training both the supervised CNNs (S+T, TGT) as well as the MRAI-NET followed by a linear classifier (NET) on the simulated data (Brainweb1.5T, Brainweb3T), 2) Multiple target training samples per tissue (randomly selected with 50 repeats) are used for training the S+T, TGT, and NET classifiers for both simulated (Brainweb3T) and real patient data (MRBrainS). The first experiment (Section 3.4) was set-up to test if only 1 target patch per tissue would be sufficient in order to learn an MR-acquisition invariant representation. If so, then calibrating a supervised segmentation algorithm for a new scanner using MRAI-NET would require only three clicks in one scan acquired with a new scanner. The second experiment (Section 3.5) illustrates the performance of the MRAI-NET compared to the TGT, and NET classifiers when adding more target training samples (Figure 7). Results of us-

ing 1 patch per tissue and 100 patches per tissue from the target subject for training are shown in Figures 8-10. Implementation and optimization details and other practical considerations with respect to MRAI-NET are described in Appendix C.

3.1. MR acquisition invariance measure

The \mathcal{H} -divergence can be used as a measure of the discrepancy between the source and target scanner data sets [19, 20, 21]. This divergence relies on the ability of a classifier to distinguish between domains. If a classifier is not able to distinguish source from target, i.e. has a test error of 1/2, then invariance is achieved. Unfortunately, the original \mathcal{H} -divergence is a measure between distributions and not samples. Since we only have samples, we use its proxy instead: the \mathcal{A} -distance [20, 21], as used in [22, 23]. The proxy \mathcal{A} -distance, denoted by $d_{\mathcal{A}}$, is defined as follows:

$$d_{\mathcal{A}}(x, z) = 2(1 - 2e(x, z)),$$

where e represents the test error of a classifier trained to discriminate source samples x from target samples z . An error of 0, i.e. perfect separability, corresponds to an \mathcal{A} -distance of 2 and an error 1/2, i.e. no separability (perfect invariance), corresponds to an \mathcal{A} -distance of 0. We use a linear support vector machine (SVM) as domain classifier.

3.2. Measure of preserving tissue variation

The tissue classification error is used as a measure of tissue variation preservation. The aim is to learn a linearly separable representation with MRAI-NET, to aid the number of methods that can be used for classification. Therefore, we evaluate the tissue classification error of the samples in the acquisition-invariant representation with a logistic regressor. The classifier is ℓ_2 -regularized and cross-validated for optimal regularization parameters. This classifier NET, based on the MRAI-NET, is compared to two other supervised classifiers: 1) S+T classifier: a convolutional-dense neural network (CNN) trained on samples from the source

(4 subjects) and target data (1 subject), and 2) TGT classifier: a CNN trained on samples from the target data (1 subject). In order to ensure that differences in performance between S+T, NET and TGT are not due to differences between classifiers, the MRAI-NET (Figure 2) neural network architecture was used for the S+T and TGT classifiers as well.

3.3. Data

To be able to provide a proof of principle, we simulated different MR acquisitions from various anatomical models of the human brain [24, 25], using an MRI simulator (SIMRI [26, 27, 25]). The anatomical models consist of transverse slices of 20 normal brains and are publicly available through Brainweb¹. These models were used as input for the MRI simulator. For the experiments, we simulated two acquisition types: 1) Brainweb1.5T, a standard gradient-echo acquisition protocol for a 1.5 Tesla scanner (c.f. [28]), and 2) Brainweb3T, a standard gradient-echo protocol for a 3.0 Tesla scanner (c.f. [29]). Table 1 describes the parameters used for the simulation: magnetic field strength (B0), flip angle (θ), repetition time (TR), echo time (TE). Magnetic field inhomogeneities and voxel inhomogeneity (partial volume effects) were not included in the simulation. Appendix A describes the nuclear magnetic resonance (NMR)

Table 1: SIMRI Acquisition parameters for the simulation of the Brainweb1.5T and Brainweb3.0T data sets.

	B0	θ	TR	TE
Brainweb1.5T	1.5 Tesla	20°	13.8 ms	2.8 ms
Brainweb3.0T	3.0 Tesla	90°	7.9 ms	4.5 ms

relaxation times for the tissues in the Brainweb anatomical models, for 1.5 and 3.0 Tesla field strengths. The tissues in the anatomical models are grouped into "background" (BKG), "cerebrospinal fluid" (CSF), "gray matter" (GM), and "white matter" (WM) to compose the ground truth segmentation labels for the

¹<http://www.bic.mni.mcgill.ca/brainweb/>

simulated scans. The simulations result in images of 256 by 256 pixels, with a 1.0x1.0mm resolution. Figures 5a and 5b show examples of the Brainweb1.5T and Brainweb3T scan of the same subject. For all scans, we used a brain mask to strip the skull. In order to test the proposed method on real data, we use

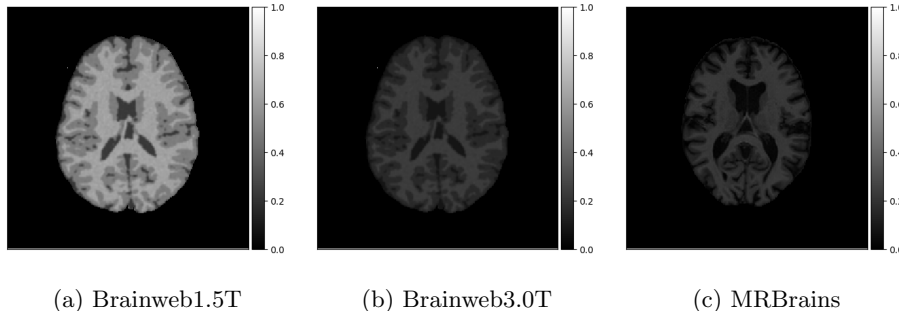


Figure 5: Example of an MRI scan of a Brainweb anatomical model simulated with SIMRI with a 1.5T protocol (a) and a 3T protocol (b), and a real patient scan (MRBrainS) acquired with a 3T protocol (c).

the publicly available training data (5 subjects) from the MRBrainS challenge². The acquisition parameters used for simulating the Brainweb3.0T are based on the MRBrainS acquisition protocol (3T scanner, gradient-echo, $B_0 = 3.0$ T, $\theta = 90^\circ$ flip angle, TE = 4.5ms, and TR = 7.9ms). Figure 5c shows an example of an MRBrainS scan. Again, a brain mask is used to strip the skull.

3.4. Experiment 1: One training target sample per tissue

The first experiment with the simulated data tests the scenario described at the beginning of this section. Suppose a supervised classification algorithm trained on one scanner needs to be calibrated for a new scanner, would this be possible with three clicks (1 for each tissue type) using MRAI-NET? Therefore we manually selected 1 sample for each tissue in the target scan (1 subject) and used this data to learn the acquisition-invariant representation using MRAI-NET. After which the three classifiers, NET (linear classifier after MRAI-NET),

²<http://mrbrains13.isi.uu.nl/Figure>

S+T (supervised CNN trained on source patches and 3 target patches), and TGT (supervised CNN trained on 3 target patches) were applied to the target test data. For comparison, we repeated this experiment with randomly selected target patches. Table 2 lists the tissue classification errors of the three classifiers and the proxy \mathcal{A} -distance between the source and target patches before (RAW) and after (REP) applying MRAI-NET. Due to random extraction of the source patches from Brainweb1.5T (4 subjects), the experiments were repeated 10 times and the average is reported with the standard error of the mean between brackets.

Table 2: Manually versus randomly selecting 1 target patch per tissue from 1 subject. (Left) Tissue classification error is reported for NET (linear classifier after MRAI-NET), S+T (supervised CNN trained on source patches and 1 target patch per tissue), and TGT (supervised CNN trained on 1 target patch per tissue) tested on the target test data. (Right) Proxy \mathcal{A} -distance between the original source and target patches (RAW) and the source and target patches after applying MRAI-NET (REP).

	S+T	NET	TGT	RAW	REP
manual	0.631 (.02)	0.223 (.01)	0.613 (.01)	1.88 (.01)	0.26 (.05)
random	0.667 (.02)	0.250 (.02)	0.610 (.06)	1.91 (.01)	0.41 (.06)

Figure 6 displays the manually selected patches and their position within the image. For both the S+T and TGT classifier, one target patch per tissue is insufficient to achieve good tissue classification performance (2 (top row): 0.631 and 0.613). However, the NET classifier performs considerably better (0.223), using only one target patch per tissue. The proxy \mathcal{A} -distance also drops from near perfect separability (1.88) to near invariance (0.26). Randomly selecting (10 repeats) 1 target patch per tissue (Table 2 (bottom row)), shows worse performance of the NET classifier, for both the classification error (0.250) as well as the \mathcal{A} -distance (0.41). Suggesting that purposive (information rich) sampling beats random sampling in this case.

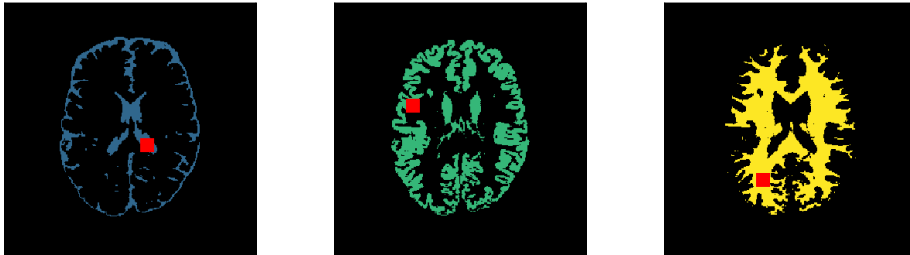


Figure 6: Locations of the manually selected target patches (red squares): Blue = cerebrospinal fluid, green = gray matter, yellow = white matter.

3.5. Experiment 2: Multiple training target samples per tissue

The second experiment tests the performance when adding more target training samples, for both simulated (Brainweb3T) and real patient data (MR-BrainS). We set-up the following sub-experiments: 2.1) Experiment on simulated data with two different acquisition protocols (Source: Brainweb1.5T, Target: Brainweb3T), 2.2) Experiment on 1.5T simulated data and 3T real data (Source: Brainweb1.5T, Target: MRBrainS), 2.3) Experiment on 3T simulated data and 3T real data (Source: Brainweb3T, Target: MRBrainS). Each of these experiments are repeated 50 times, and we report the average along with the standard error of the mean. Results are shown that vary from using only 1 patch per tissue from the target domain subject to using more than 1000 patches per tissue from the target domain subject for training both the supervised CNNs (S+T, TGT) as well as the MRAI-NET followed by a linear classifier (NET). Figure 7 shows the performance (both tissue classification error as well as proxy \mathcal{A} -distance) as a function of the number of used target training samples.

Figure 7 (left) shows the proxy \mathcal{A} -distance between the source and target samples for all three experiments. The proxy \mathcal{A} -distance for experiments 2.1 and 2.2 shows that in the original representation (raw; red line), the source and target distributions lie far apart (high distance). This illustrates the difference in acquisition protocol (1.5T versus 3T). After applying MRAI-NET the proxy \mathcal{A} -distance drops drastically (rep; blue line) showing that the network managed to learn an MR-acquisition invariant representation. Adding more target training

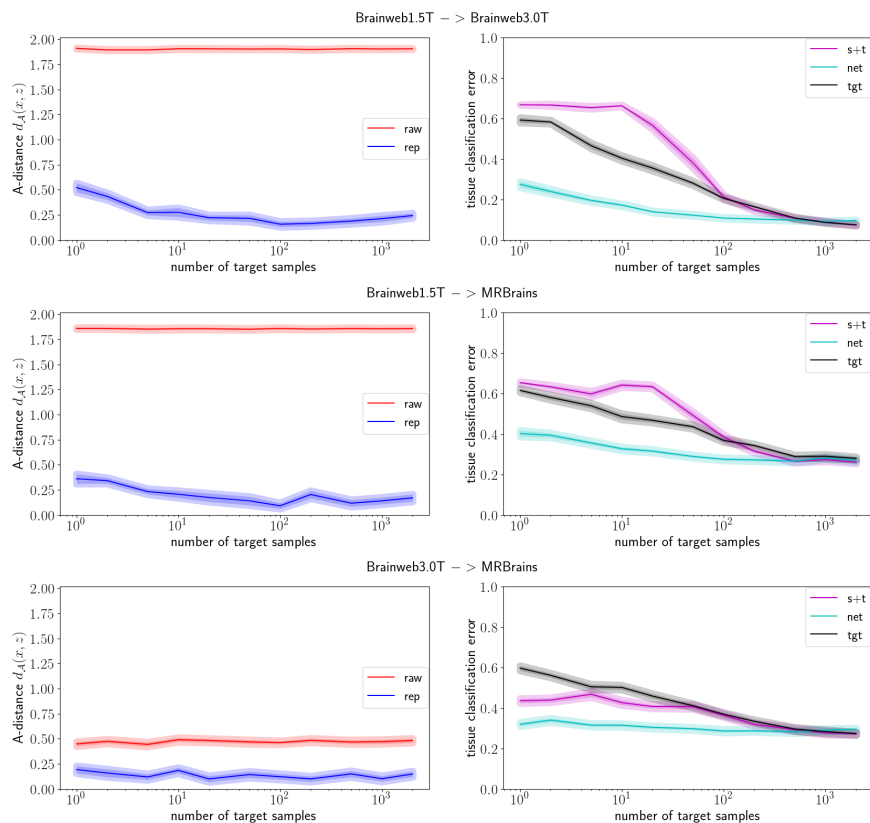


Figure 7: Graphs showing the effect of adding more labeled samples from the target scanner for training the networks in all three experiments: 2.1) Source: Brainweb1.5T, Target: Brainweb3.0T, 2.2) Source: Brainweb1.5T, Target: MRBrainS, 2.3) Source: Brainweb3.0T, Target: MRBrainS. (Left) **Measure of acquisition invariance:** Proxy A-distance between source and target scanner patches before (RAW) and after (REP) learning the MRAI representation (a smaller distance denotes more acquisition invariance). (Right) **Measure of preserving tissue variation:** Tissue classification error for the three classifiers s+t (supervised CNN trained on patches from source and target scanners), NET (MRAI-net + supervised SVM) and TGT (supervised CNN trained on patches from the target scanner). Note that the CNN architecture of the s+t and TGT classifiers is equal to the MRAI-net pipeline architecture.

samples improves the invariance up to about 100 samples, but the proxy \mathcal{A} -distance is already quite low after only using 1 target sample per tissue type for training. In experiment 2.3 the proxy \mathcal{A} -distance before applying MRAI-NET (RAW) is already much lower than in the previous two experiments, this

illustrates that the acquisition protocols are more similar to begin with (both 3T). The main difference between the distributions presumably results from simulated versus real data, since not all factors of acquisition variation are included in the simulations, most notably partial volume (0.96x0.96x3mm voxels in MRBrainS versus no partial volume in Brainweb). However, after applying MRAI-NET the proxy \mathcal{A} -distance is reduced further, again showing that MRAI-NET is able to learn an MR-acquisition invariant representation (REP), even for simulated and real data. Note that the MRBrainS data adds other modes of variation in terms of pathology and age in comparison to the Brainweb healthy adults, which could influence the tissue classification performance.

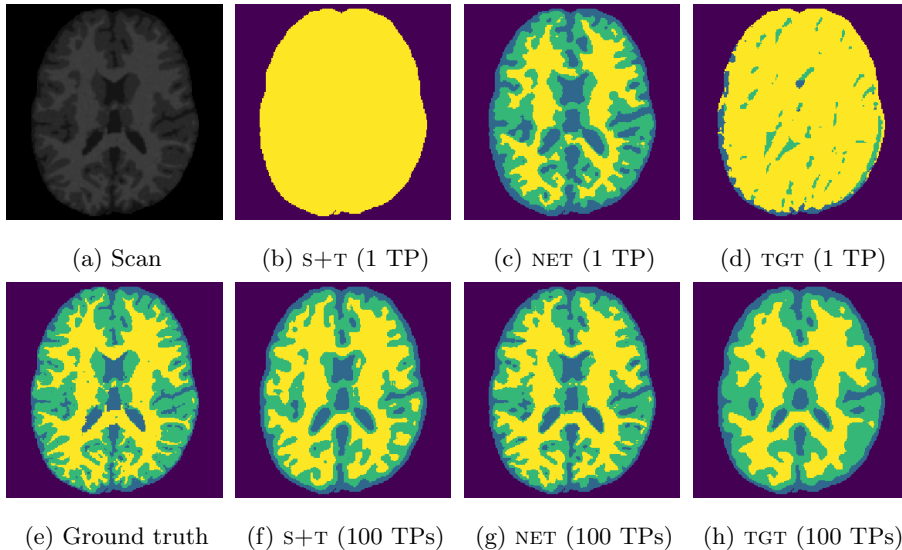


Figure 8: Example brain tissue segmentations into white matter (yellow), gray matter (green) and cerebrospinal fluid (blue) for experiment 2.1 (Source: Brainweb1.5T, Target: Brainweb3T). A simulated MRI scan of a test subject from Brainweb3T (a) is shown, with corresponding ground truth segmentation (e), and the results of applying the s+T (b,f), TGT (d,h) and proposed NET (c,g) classifiers, with either 1 or 100 target patches per tissue type used for training the classifiers (Figure 7).

Figure 7 (right) shows the tissue classification error for all three experiments. If the proxy \mathcal{A} -distance between the source and target distribution is high (experiment 2.1 and 2.2), and when using only one target sample per tissue, the

S+T classifier that uses both the source data and target data for training performs worse than the one that uses only the target data (TGT); an error of 0.667 versus 0.591, respectively. Even when adding more target samples for training, the results show that it is more beneficial to train a supervised classifier on the target data alone, instead of on both the source and target data; using 10 target samples for training, S+T achieves an error of 0.662 versus an error of 0.403 for TGT. The S+T classifier is focused on its source samples, which in this case are not informative of the target data. Given enough target samples, however, S+T starts to shift focus towards its target data and starts to match the performance of TGT: for 100 target samples, errors of 0.213 versus 0.205 respectively. If the proxy \mathcal{A} -distance between the source and target distributions is low (distributions are more similar; experiment 2.3), using the source data for training is beneficial; for 1 target sample per tissue S+T achieves an error of 0.435 and TGT an error of 0.596. In this case, the source samples are more representative of the target data and are aiding the classifier. In general, the NET classifier outperforms both the S+T and TGT classifiers: an error of 0.269 for 1 sample, 0.175 for 10 samples and 0.111 for 100 samples. MRAI-NET’s representation ensures that the source and target samples are more similar and that the source samples can be effectively used for training.

Examples of the segmentation results on one of the target test images are shown in Figure 8 for experiment 2.1, Figure 9 for experiment 2.2, and Figure 10 for experiment 2.3. Examples are shown after using 1 target patch per tissue for training, and after using 100 target patches per tissue for training. The results show that only the NET classifier is able to predict a segmentation that approaches the ground truth with only 1 target patch per tissue for training (error for experiment 2.1 = 0.269, experiment 2.2 = 0.403, experiment 2.3 = 0.320), while the S+T and TGT classifiers cannot (S+T error for experiment 2.1 = 0.667, experiment 2.2 = 0.653, experiment 2.3 = 0.435; TGT error for experiment 2.1: 0.591, experiment 2.2: 0.614, experiment 2.3 = 0.596). After using 100 patches the S+T and TGT classifiers can predict a gross segmentation of WM, GM and CSF (S+T error for experiment 2.1 = 0.213, experiment 2.2 =

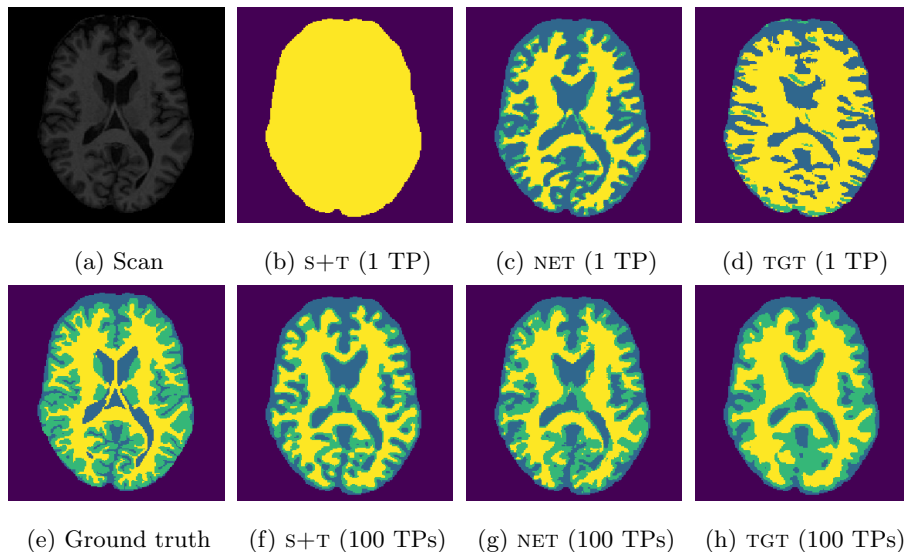


Figure 9: Example brain tissue segmentations into white matter (yellow), gray matter (green) and cerebrospinal fluid (blue) for experiment 2.2 (Source: Brainweb1.5T, Target: MRBrainS). A simulated MRI scan of a test subject from MRBrainS (a) is shown, with corresponding ground truth segmentation (e), and the results of applying the s+T (b,f), TGT (d,h) and proposed NET (c,g) classifiers, with either 1 or 100 target patches per tissue type used for training the classifiers (Figure 7).

0.384, experiment 2.3 = 0.363; TGT error for experiment 2.1: 0.205, experiment 2.2: 0.368, experiment 2.3 = 0.368), but the NET classifier prediction shows more details and a lower tissue classification error (error for experiment 2.1 = 0.111, experiment 2.2 = 0.276, experiment 2.3 = 0.284).

4. Discussion

In this paper, we proposed a method to learn an MR acquisition invariant (MRAI) representation that preserves the variation between brain tissues for segmentation. Once the representation is learned using MRAI-NET, any classifier can be used to classify the brain tissues. The proposed method addresses the problem that the difference between scans acquired with two different MRI scanners or protocols can be so large that scans from one scanner are not representative

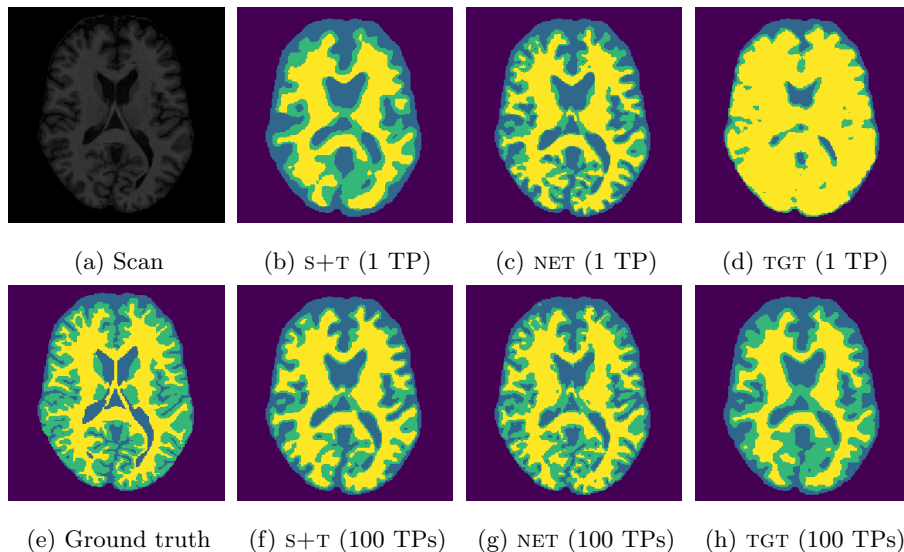


Figure 10: Example brain tissue segmentations into white matter (yellow), gray matter (green) and cerebrospinal fluid (blue) for experiment 2.3 (Source: Brainweb3T, Target: MRBrainS). A simulated MRI scan of a test subject from MRBrainS (a) is shown, with corresponding ground truth segmentation (e), and the results of applying the s+T (b,f), TGT (d,h) and proposed NET (c,g) classifiers, with either 1 or 100 target patches per tissue type used for training the classifiers (Figure 7).

of scans from another scanner. This difference does not affect assessment by human vision (e.g. radiologists can perform diagnostic work-up on both), but it does affect computer vision. To get insight into the difference between scans and to assess the performance of MRAI-NET to reduce this difference (achieve invariance), the proxy \mathcal{A} -distance measure between source and target patches was used. The experiments (Figure 7) show that this is a good measure to determine the difference between source and target acquisition, and might be used to predict classifier performance of a source classifier. Note that this measure does not require any tissue labels, and can thus be used as a general measure of distance between scanners. It merely requires source patches to be labeled as source, and target patches to be labeled as target. When the proxy \mathcal{A} -distance is low (Figure 7 bottom row) the source (s+T) classifier outperforms the target (TGT) classifier when a small number of target training patches are used. When

the proxy \mathcal{A} -distance is large the TGT classifier outperforms the S+T classifier, even when one target training patch per tissue is used. This suggests that if the proxy \mathcal{A} -distance is large (source data is not representative of target data), a source classifier trained on the source data should not be applied to the target data. Ground truth labels on the source data that are labor-intensive to acquire can in this case not be used for the target data. However, since MRAI-NET learns a representation that reduces the acquisition difference between source and target scanner the proxy \mathcal{A} -distance is drastically reduced. Therefore the NET classifier outperforms both the S+T and TGT classifiers, when a small number of target training samples is available, and leverages the source ground truth labels.

Due to the complexity of the problem addressed in this paper, simulated data was used to provide a proof of principle. Ideal real data would require the same subject to be scanned on different scanners with different protocols, after which the scans should be manually segmented to obtain the ground truth for both scans. However, inter-observer variability would add an extra layer of variation. To test MRAI-NET on real data, the MRBrainS challenge data was used. Although, additional layers of variation include resolution, population and manual segmentation protocol, the experiments (Figure 7) show that the MRAI-NET performance on real data follows the same pattern as its performance on simulated data, be it with a higher classification error due to additional factors of variation.

A limitation of the proposed method is that learning an MRAI representation with MRAI-NET, will not necessarily work well on data sets with poor contrast between tissues. In that case, the network will both push and pull points in the overlap. Since these actions will mostly cancel each other out, the network will not be able to reduce acquisition-variation without sacrificing tissue variation, and vice versa.

Another limitation is that the proposed MRAI-NET requires at least 1 sample per tissue from the target scanner. This is not an unreasonable request, as it is not hard to find at least 1 patch per tissue (Section 3.4) in only one sub-

ject scanned with the target scanner. However, it may be possible to perform the similar/dissimilar labeling based on assumptions instead. For instance, if one assumes that the registration between two scans is accurate and that the subject-variation is not too large, then one could assume that target patches at certain locations are the same tissue as the source patches at these locations. Hence, those voxels could be used for the similarity-labeling process.

The proposed representation learning method could be used to reduce any type of variation, by adjusting the way that the similar and dissimilar pairs are defined. For example, registration, which can be viewed as variation in position, might be approached in a similar manner [30]. Key is to identify the forms of variation, determine which variation should be preserved and which should be reduced, and to find a way to label them as similar or dissimilar accordingly.

5. Conclusion

In this paper we addressed one of the major challenges of supervised voxel classification, i.e. generalization to data that is not representative of the training data. We provided a proof of principle for learning an MR acquisition invariant representation that reduces the variation between MRI scans acquired with different scanners or acquisition protocols, while preserving the variation between brain tissues. We showed that the proposed MR-AI-NET is able to learn an MR acquisition invariant representation (low proxy \mathcal{A} -distance), and outperform supervised convolution neural networks trained on patches from the source or target scanners for tissue classification, when little target training patches are available. By reducing the acquisition related variation using MR-AI-NET, the ground truth labels from the source data can be reused for the target data, since the source and target data are mapped to the same representation achieving generalization.

6. Acknowledgements

The research of A.M. Mendrik was financially supported by IMDI Grant 104002002 (Brainbox) from ZonMw, the Netherlands Organisation for Health Research and Development. W.M. Kouw was supported by the Netherlands Organization for Scientific Research (NWO; grant 612.001.301).

Appendix A Nuclear Magnetic Resonance relaxation times

SIMRI requires NMR relaxation times for tissues based on particular magnetic static field strengths [26]. We performed a literature study for the T1 and T2 relaxation times, the results of which are listed in Table 3. The proton density values ρ stem from [31]. The 3.0T CSF parameters were interpolated using an exponential function fit ([32] justifies an exponential function based on physical properties). We equate connective tissue to glial matter (90% of the brain's connective tissue system is glial matter³).

³<http://www.neuroplastix.com/styled-2/page139/styled-42/brainsconnectivetissue.html>

Table 3: NMR relaxation times for brain tissue (IT’IS database).

^a Glial matter values are unknown and are imputed with gray matter values.

^b T2 values for cortical bone are actually T2* values (UTE seq).

^c Equated to glial matter (see text).

^d 3.0T T2 relaxation time is from dermis, other values are from hypodermis.

Tissue	ρ	T1(1.5T)	T2(1.5T)	T1(3.0T)	T2(3.0T)	Ref
CSF	100 (0)	4326 (0)	791 (127)	4313 (0)	503 (64)	[32, 33, 34, 35]
GM	86 (.4)	1124 (24)	95 (8)	1820 (114)	99 (7)	[36]
WM	77 (3)	884 (50)	72 (4)	1084 (45)	69 (3)	[36]
Fat	100 (0)	343 (37)	58 (4)	382 (13)	68 (4)	[37]
Muscle	100 (0)	629 (50)	44 (6)	832 (62)	50 (4)	[36, 38]
Skin ^d	100 (0)	230 (8)	35 (4)	306 (18)	22 (0)	[39, 40, 38]
Skull ^b	0 (0)	200 (0)	.46 (0)	223 (11)	.39 (.02)	[41, 42]
Glial ^a	86 (0)	1124 (24)	95 (8)	1820 (114)	99 (7)	[33, 36]
Conn. ^c	77 (0)	1124 (24)	95 (8)	1820 (114)	99 (7)	[36]

Appendix B Balance between similar and dissimilar

The margin parameter m in the dissimilar loss function, $\ell_{\text{dis}}(f | a, b) = \max(0, m - \|f(a) - f(b)\|_p)$, is important as it balances the actions of pushing and pulling between pairs. For small values, ℓ_{dis} will be much smaller than ℓ_{sim} and the network will focus on pulling pairs together. For large values, ℓ_{dis} will always be much larger than ℓ_{sim} and network will focus on pushing pairs apart. Figure 11 plots a synthetic setting with the outcome of using three different values for the margin parameter. The left figure show two 2-dimensional data sets, one with red versus blue crosses and the other with red versus blue squares. The right figures show validation samples fed through three networks with different values for the margin parameter. Firstly, the right top figure displays the result of using a margin parameter of 0: the network does not suffer *any* loss by making pairs of samples of different tissues too similar and consequently maps everything to a single point. Secondly, the right middle figure

shows an appropriate choice for the margin, where the two data sets overlap and where red and blue points are separated. Lastly, the right bottom figure shows what happens when a large margin parameter is used: it focuses almost entirely on separating red versus blue and is not making the data sets more similar.

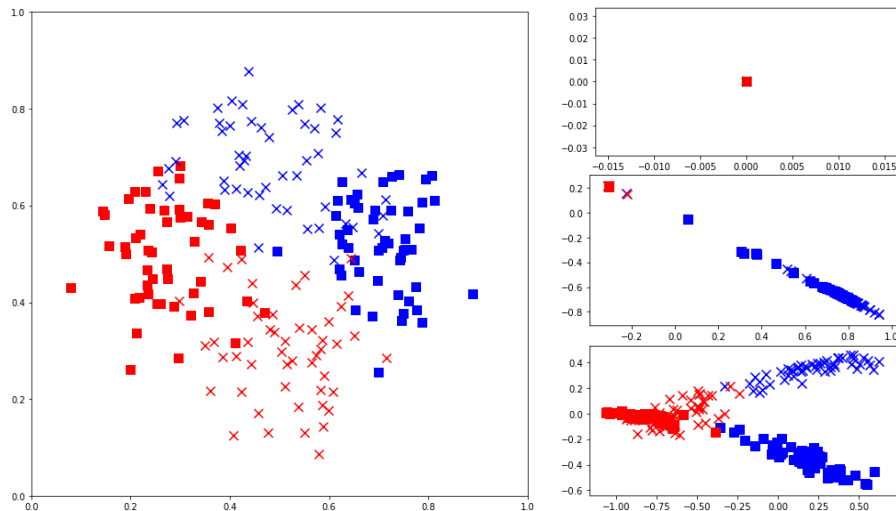


Figure 11: Effect of the margin hyperparameter. (Left) Two synthetic binary data sets, with markers indicating scanners and colors tissues. (Right) Representation found by a network with a margin of 0 (top), a margin of 1 (middle) and a margin of 10 (bottom).

. Additionally, the optimal value for the margin parameter is affected by the number of similar versus dissimilar pairs. If there are twice as many similar pairs, then their loss will be twice as large as well and the network will focus more on pulling pairs together. Overall, the more similar pairs there are, the larger the margin parameter will need to be.

Appendix C Practical considerations

Our method is implemented in a combination of Tensorflow⁴ and Keras⁵ [43, 44]. All experiments in this paper are performed with the default back-

⁴<https://www.tensorflow.org/>

⁵<https://keras.io/>

propagation algorithm ("rmsprop"), which normalizes the gradient update with a running average of itself [45]. Its default parameters are: a learning rate of 0.001, a ρ of 0.9, an ϵ of 1e-08, and a weight decay factor of 0.0 (see [45] for more details on optimizer parameters). "rmsprop" is based on stochastic gradient descent, which splits the dataset into batches and updates the networks parameters after processing each batch. An epoch is the number of times the optimization procedure splits the training set into batches. The number of epochs can not be too large. Otherwise, the network starts to overfit to the specific target subject from which the target patches originated. This behavior could be combated by including patches from other subjects in the target scanner. Alternatively, "early stopping" techniques could be used that maintain a held-out validation set of pairs of samples and check when the validation loss starts to increase.

It is important that the batches are well-mixed with respect to the 6 types of pairs outlined in Section 2.2. If this is not the case, such as when one batch mostly consists of similar gray-matter patches and another batch consists mostly of dissimilar gray-matter / white-matter patches, then the network tends to push and pull in the same direction. These actions cancel each other out. The overall effect of having too many uniform batches is that the optimization procedure is slowed down.

During training, we apply an l_2 -regularization of 0.001 to every layer with weights. Regularization punishes the size of the weights, which prevents model over-complexity. In our experiments, the regularization parameter could be increased/decreased by two orders of magnitude with little effect on the networks performance. It is however always necessary to include *some* regularization as there is not only the danger of overfitting to training data but also the danger to overfitting to the specific target subject used during training.

In Section 2.1 we specified the Siamese loss as the networks objective function. The input of this loss consists of a pairwise distance, for which we chose an L^1 -norm. There are 2 reasons for this: the first is that L^p -norms with larger values for p concentrate densely in high-dimensional spaces [46]. Concentration

means that the differences between pairwise distances of a set of points become smaller as the number of dimensions increases. This is a problem because the actions of pulling and pushing will not sufficiently decrease the distance between similar pairs or sufficiently increase the distance between dissimilar pairs. The second reason is that the gradient of the L^1 -norm is constant, while the gradient of an L^p -norms with $p > 1$ are functions of the distance [47]. Gradients of norms with large p 's become smaller as the distance between pairs becomes smaller, which means the incentive for the network to pull pairs closer decreases. A constant gradient ensures that there will also be a constant incentive to pull similar pairs closer together. Considering that we want our representation to be truly invariant, we want the network to continue to pull similar pairs together until they are as close as possible.

References

References

- [1] J. C. Bezdek, L. Hall, L. Clarke, Review of MR image segmentation techniques using pattern recognition, *Medical Physics* 20 (4) (1993) 1033–1048.
- [2] A. P. Zijdenbos, B. M. Dawant, Brain segmentation and white matter lesion detection in MR images, *Critical Reviews in Biomedical Engineering* 22 (5-6) (1994) 401–465.
- [3] L. Clarke, R. Velthuizen, M. Camacho, J. Heine, M. Vaidyanathan, L. Hall, R. Thatcher, M. Silbiger, MRI segmentation: methods and applications, *Magnetic Resonance Imaging* 13 (3) (1995) 343–368.
- [4] N. Saeed, Magnetic resonance image segmentation using pattern recognition, and applied to image registration and quantitation, *NMR in Biomedicine* 11 (4-5) (1998) 157–167.
- [5] D. L. Pham, C. Xu, J. L. Prince, Current methods in medical image segmentation, *Annual Review of Biomedical Engineering* 2 (1) (2000) 315–337.

- [6] J. S. Suri, S. Singh, L. Reden, Computer vision and pattern recognition techniques for 2-D and 3-D MR cerebral cortical segmentation (part i): a state-of-the-art review, *Pattern Analysis & Applications* 5 (1) (2002) 46–76.
- [7] J. S. Duncan, X. Papademetris, J. Yang, M. Jackowski, X. Zeng, L. H. Staib, Geometric strategies for neuroanatomic analysis from MRI, *Neuroimage* 23 (2004) S34–S45.
- [8] M. A. Balafar, A. R. Ramli, M. I. Saripan, S. Mashohor, Review of brain MRI image segmentation methods, *Artificial Intelligence Review* 33 (3) (2010) 261–274.
- [9] A. Giorgio, N. De Stefano, Clinical use of brain volumetry, *Journal of Magnetic Resonance Imaging* 37 (1) (2013) 1–14.
- [10] A. van Opbroek, M. Ikram, M. Vernooij, M. De Bruijne, Transfer learning improves supervised image segmentation across imaging protocols, *IEEE Transactions on Medical Imaging* 34 (5) (2015) 1018–1030.
- [11] P. Moeskops, M. A. Viergever, A. M. Mendrik, L. S. de Vries, M. J. Benders, I. Išgum, Automatic segmentation of MR brain images with a convolutional neural network, *IEEE Transactions on Medical Imaging* 35 (5) (2016) 1252–1261.
- [12] H. Chen, Q. Dou, L. Yu, J. Qin, P.-A. Heng, Voxresnet: Deep voxelwise residual networks for brain segmentation from 3D MR images, *NeuroImage*.
- [13] Y. Bengio, A. Courville, P. Vincent, Representation learning: A review and new perspectives, *IEEE Transactions on Pattern Analysis and Machine Intelligence* 35 (8) (2013) 1798–1828.
- [14] A. van Opbroek, M. A. Ikram, M. W. Vernooij, M. de Bruijne, Supervised image segmentation across scanner protocols: A transfer learning approach, in: *Machine Learning in Medical Imaging*, Springer, 2012, pp. 160–167.

- [15] Y. Bengio, et al., Learning deep architectures for AI, *Foundations and Trends® in Machine Learning* 2 (1) (2009) 1–127.
- [16] J. Bromley, J. W. Bentz, L. Bottou, I. Guyon, Y. LeCun, C. Moore, E. Säckinger, R. Shah, Signature verification using a siamese time delay neural network, *International Journal of Pattern Recognition and Artificial Intelligence* 7 (04) (1993) 669–688.
- [17] R. Hadsell, S. Chopra, Y. LeCun, Dimensionality reduction by learning an invariant mapping, in: *Computer Vision and Pattern Recognition, IEEE Computer Society Conference on*, Vol. 2, IEEE, 2006, pp. 1735–1742.
- [18] Y. LeCun, F. J. Huang, L. Bottou, Learning methods for generic object recognition with invariance to pose and lighting, in: *Computer Vision and Pattern Recognition, IEEE Computer Society Conference on*, Vol. 2, IEEE, 2004, pp. II–97–104.
- [19] D. Kifer, S. Ben-David, J. Gehrke, Detecting change in data streams, in: *Proceedings of the Thirtieth International Conference on Very Large Data Bases*, Vol. 30, VLDB Endowment, 2004, pp. 180–191.
- [20] S. Ben-David, J. Blitzer, K. Crammer, F. Pereira, Analysis of representations for domain adaptation, in: *Advances in Neural Information Processing Systems*, 2007, pp. 137–144.
- [21] S. Ben-David, J. Blitzer, K. Crammer, A. Kulesza, F. Pereira, J. W. Vaughan, A theory of learning from different domains, *Machine Learning* 79 (1) (2010) 151–175.
- [22] X. Glorot, A. Bordes, Y. Bengio, Domain adaptation for large-scale sentiment classification: A deep learning approach, in: *Proceedings of the 28th International Conference on Machine Learning*, 2011, pp. 513–520.
- [23] Y. Ganin, E. Ustinova, H. Ajakan, P. Germain, H. Larochelle, F. Laviolette, M. Marchand, V. Lempitsky, Domain-adversarial training of neural networks, *Journal of Machine Learning Research* 17 (59) (2016) 1–35.

- [24] D. L. Collins, A. P. Zijdenbos, V. Kollokian, J. G. Sled, N. J. Kabani, C. J. Holmes, A. C. Evans, Design and construction of a realistic digital brain phantom, *IEEE Transactions on Medical Imaging* 17 (3) (1998) 463–468.
- [25] B. Aubert-Broche, M. Griffin, G. B. Pike, A. C. Evans, D. L. Collins, Twenty new digital brain phantoms for creation of validation image data bases, *IEEE Transactions on Medical Imaging* 25 (11) (2006) 1410–1416.
- [26] H. Benoit-Cattin, G. Collewet, B. Belaroussi, H. Saint-Jalmes, C. Odet, The SIMRI project: a versatile and interactive MRI simulator, *Journal of Magnetic Resonance* 173 (1) (2005) 97–115.
- [27] B. Aubert-Broche, A. C. Evans, L. Collins, A new improved version of the realistic digital brain phantom, *NeuroImage* 32 (1) (2006) 138–145.
- [28] M. A. Ikram, A. van der Lugt, W. J. Niessen, P. J. Koudstaal, G. P. Krestin, A. Hofman, D. Bos, M. W. Vernooij, The rotterdam scan study: design update 2016 and main findings, *European Journal of Epidemiology* 30 (12) (2015) 1299–1315.
- [29] A. M. Mendrik, K. L. Vincken, H. J. Kuijf, M. Breeuwer, W. H. Bouvy, J. De Bresser, A. Alansary, M. De Bruijne, A. Carass, A. El-Baz, et al., MRBrainS challenge: Online evaluation framework for brain image segmentation in 3T MRI scans, *Computational Intelligence and Neuroscience*.
- [30] M. Simonovsky, B. Gutiérrez-Becker, D. Mateus, N. Navab, N. Komodakis, A deep metric for multimodal registration, in: *International Conference on Medical Image Computing and Computer-Assisted Intervention*, Springer, 2016, pp. 10–18.
- [31] D. Yoder, E. Changchien, C. B. Paschal, J. M. Fitzpatrick, MRI simulator with static field inhomogeneity, in: *Medical Imaging, International Society for Optics and Photonics*, 2002, pp. 592–603.

- [32] R. M. Kroeker, R. M. Henkelman, Analysis of biological NMR relaxation data with continuous distributions of relaxation times, *Journal of Magnetic Resonance* 69 (2) (1986) 218–235.
- [33] K. H. Cheng, In vivo tissue characterization of human brain by chisquares parameter maps: multiparameter proton T2-relaxation analysis, *Magnetic Resonance Imaging* 12 (7) (1994) 1099–1109.
- [34] W. D. Rooney, G. Johnson, X. Li, E. R. Cohen, S.-G. Kim, K. Ugurbil, C. S. Springer, Magnetic field and tissue dependencies of human brain longitudinal $^1\text{H}_2\text{O}$ relaxation in vivo, *Magnetic Resonance in Medicine* 57 (2) (2007) 308–318.
- [35] S. Piechnik, J. Evans, L. Bary, R. G. Wise, P. Jezzard, Functional changes in CSF volume estimated using measurement of water T2 relaxation, *Magnetic Resonance in Medicine* 61 (3) (2009) 579–586.
- [36] G. J. Stanisz, E. E. Odrobina, J. Pun, M. Escaravage, S. J. Graham, M. J. Bronskill, R. M. Henkelman, T1, T2 relaxation and magnetization transfer in tissue at 3T, *Magnetic Resonance in Medicine* 54 (3) (2005) 507–512.
- [37] C. M. De Bazelaire, G. D. Duhamel, N. M. Rofsky, D. C. Alsop, MR imaging relaxation times of abdominal and pelvic tissues measured in vivo at 3.0 T: preliminary results, *Radiology* 230 (3) (2004) 652–659.
- [38] J. K. Barral, N. Stikov, E. Gudmundson, P. Stoica, D. G. Nishimura, Skin T1 mapping at 1.5T, 3T, and 7T, in: *Proceedings of the 17th Annual Meeting of ISMRM, 2009*, p. 4451.
- [39] S. Richard, B. Querleux, J. Bittoun, I. Idy-Peretti, O. Jolivet, E. Cermakova, J.-L. Lévêque, In vivo proton relaxation times analysis of the skin layers by magnetic resonance imaging, *Journal of Investigative Dermatology* 97 (1) (1991) 120–125.
- [40] H. K. Song, F. W. Wehrli, J. Ma, In vivo MR microscopy of the human skin, *Magnetic Resonance in Medicine* 37 (2) (1997) 185–191.

- [41] I. L. Reichert, M. D. Robson, P. D. Gatehouse, T. He, K. E. Chappell, J. Holmes, S. Girgis, G. M. Bydder, Magnetic resonance imaging of cortical bone with ultrashort TE pulse sequences, *Magnetic Resonance Imaging* 23 (5) (2005) 611–618.
- [42] J. Du, M. Carl, M. Bydder, A. Takahashi, C. B. Chung, G. M. Bydder, Qualitative and quantitative ultrashort echo time (UTE) imaging of cortical bone, *Journal of Magnetic Resonance* 207 (2) (2010) 304–311.
- [43] M. Abadi, P. Barham, J. Chen, Z. Chen, A. Davis, J. Dean, M. Devin, S. Ghemawat, G. Irving, M. Isard, M. Kudlur, J. Levenberg, R. Monga, S. Moore, D. G. Murray, B. Steiner, P. Tucker, V. Vasudevan, P. Warden, M. Wicke, Y. Yu, X. Zheng, Tensorflow: A system for large-scale machine learning, in: *12th USENIX Symposium on Operating Systems Design and Implementation (OSDI 16)*, 2016, pp. 265–283.
- [44] F. Chollet, et al., Keras, <https://github.com/fchollet/keras> (2015).
- [45] L. Bottou, Stochastic gradient descent tricks, in: *Neural Networks: Tricks of the Trade*, Springer, 2012, pp. 421–436.
- [46] A. Flexer, D. Schnitzer, Choosing ℓ^p norms in high-dimensional spaces based on hub analysis, *Neurocomputing* 169 (2015) 281–287.
- [47] S. Boyd, L. Vandenberghe, *Convex optimization*, Cambridge University Press, 2004.